

Computing extracellular electrical potentials from neuronal simulations

Geir Halnes^{a,b}, Torbjørn V. Ness^a, Solveig Næss^b, Klas H. Pettersen^c, Gaute T. Einevoll^{a,b,d,*}

^a*Faculty of Science and Technology, Norwegian University of Life Sciences, Ås, Norway*

^b*Center for Integrative Neuroplasticity, University of Oslo, Oslo, Norway*

^c*Norwegian Artificial Intelligence Research Consortium, Oslo, Norway*

^d*Department of Physics, University of Oslo, Oslo, Norway*

Abstract

[GH: Vet ikke hva forfatterordningen skal vaere, men vi faar se det an etter hvert, og bestemme utifra hvem som har jobbet mest med manus. For oøyeblikket leder jeg, men jeg tror jeg satser paa at kanskje Torbjørn fosser forbi etter hvert.] [TVN: Just to be sure: If we make figures for this chapter, we have the right to re-use those wherever we like?] [TVN: Giugliano: max 15-20 pages, by February 2020]

Keywords: extracellular potentials, LFP, EEG, ECoG, electrodiffusion

Contents

1	Introduction	2
2	From electrodiffusion to volume conductor theory	3
2.1	Ion concentration dynamics	4
2.2	Electrodynamics	5
2.3	Volume conductor theory	6
2.3.1	Current-dipole approximation	7
2.3.2	Assumptions in volume conductor theory	8
2.4	Modeling electrodes	9
3	Single-cell contributions to extracellular potentials	10
4	Intra-cortical extracellular potentials from neural populations	10
4.1	Local field potentials	11
4.2	MUA	13
5	ECoG and EEG	13
5.1	Head models	14
6	Discussion	15

*correspondence: gaute.einevoll@nmbu.no

1 **1. Introduction**

2 Arguably, most of what we have learned about the mechanisms by which neurons and networks
3 operate in living brains comes from recordings of extracellular potentials. In such recordings, electri-
4 cal potentials are measured by electrodes that are either placed between cells in brain tissue (spikes,
5 LFPs), at the cortical surface (ECoG, electrocorticography), or at the scalp (EEG, electroencephalo-
6 grapy) (Figure 1). Spikes, the high-frequency part of the extracellular potentials recorded inside gray
7 matter, are reliable signatures of neuronal action potentials, and spike measurements have been
8 instrumental in mapping out, for example, receptive fields accounting for how sensory stimuli are
9 represented in the brain. The analysis of the LFP signal, the low-frequency part of electrical po-
10 tentials recorded inside gray matter, as well as the ECoG, and EEG signals is less straightforward.
11 Interpretation of the signal in terms of the underlying neural activity has been difficult, and most
12 analysis of the data has been purely statistical [Nunez and Srinivasan, 2006; Buzsáki et al., 2012;
13 Einevoll et al., 2013a; Ilmoniemi and Sarvas, 2019].

14 The tradition of physics is different. Here candidate hypotheses are typically formulated as spe-
15 cific mathematical models, and predictions computed from the models are compared with experi-
16 ments. In neuroscience this approach has been used to model activity in individual neurons using,
17 for example, biophysically detailed neuron models based on the cable equation formalism (see, e.g.,
18 Koch [1999]; Sterratt et al. [2011]). Here the models have largely been developed and tested by
19 comparison with membrane potentials recorded by intracellular electrodes in *in vitro* settings (but
20 see Gold et al. [2007]). To pursue this mechanistic approach to network models in layered struc-
21 tures such as cortex or hippocampus, one would like to compare model predictions with all available
22 experimental data, that is, not only spike times recorded for a small subset of the neurons, but also
23 population measures such as LFP, ECoG and EEG signals [Einevoll et al., 2019]. This chapter
24 addresses how to model such electrical population signals from neuron and network models.

25 In addition to allowing for validation on large-scale network models mimicking specific biologi-
26 cal networks, e.g., Reimann et al. [2013]; Markram et al. [2015]; Billeh et al. [2020], we believe a
27 key application is to generate model-based benchmarking data for validation of data analysis meth-
28 ods [Denker et al., 2012]. One example is the use of such benchmarking data to develop and test
29 spike-sorting methods Hagen et al. [2016]; Buccino and Einevoll [2019] or test methods for localiza-
30 tion and classification of cell types [Delgado Ruz and Schultz, 2014; Buccino et al., 2018]. Another
31 example is testing of methods for analysis of LFP signals, such as CSD analysis [Pettersen et al.,
32 2008; Łęski et al., 2011; Ness et al., 2015] or ICA analysis [Głabska et al., 2014], or joint analysis of
33 spike and LFP signals such as laminar population analysis (LPA) [Głabska et al., 2016].

34 The standard way to compute extracellular potentials from neural activity is a two-step pro-
35 cess [Holt and Koch, 1999; Lindén et al., 2014; Hagen et al., 2018]:

- 36 1. Compute the net transmembrane current in all neuronal segments in (networks of) biophysically-
37 detailed neuron models, and
- 38 2. use volume-conductor (VC) theory to compute extracellular potentials from the these com-
39 puted transmembrane currents.

40 This book chapter describes the origin of VC theory, that is, how it can be derived from a more de-
41 tailed electrodiffusive theory describing dynamics of ions in the extracellular media. It also provides
42 examples where our tool LFPy (LFPy.github.io) [Lindén et al., 2014; Hagen et al., 2018] is used
43 to compute spikes, LFP signals and EEG signals generated by neurons and neuronal populations.

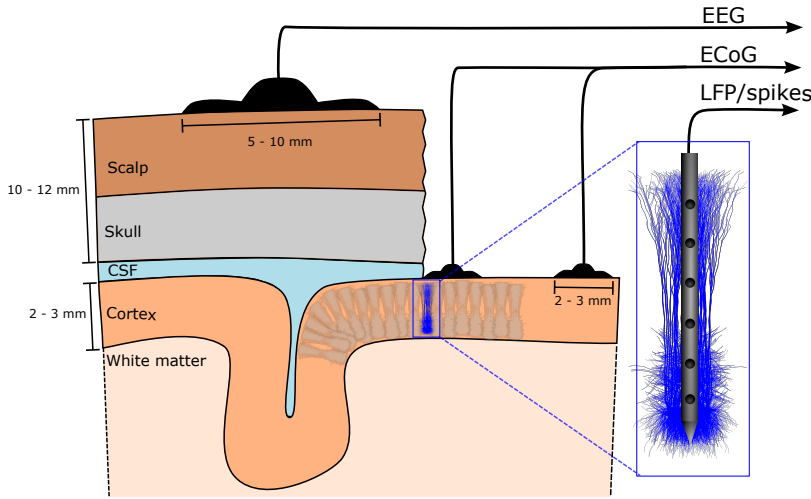


Figure 1: **LFP, ECoG and EEG.** The same basic building blocks, that is, currents caused by large numbers of synaptic input are contributing to several different measurable signals.

44 2. From electrodifusion to volume conductor theory

45 The recorded extracellular potentials are generated by electrical currents, that is, movement
 46 of ions, in the extracellular space. Such an extracellular electrical current can in principle include
 47 several components:

- 48 1. a drift component (ions migrating in electrical fields),
 49 2. a diffusion component (ions diffusing due to concentration gradients),
 50 3. an advective component (extracellular fluid flow drags ions along), and
 51 4. a displacement component (ions pile up and changes the local charge density).

52 Since the extracellular bulk fluid has very fast relaxation times and is very close to electroneutral,
 53 the latter two current components (3-4) are extremely small and are typically neglected [Grodzinsky,
 54 2011; Gratiy et al., 2017]. The diffusive component (2) is acknowledged to play an important role for
 55 voltage dynamics on a tiny spatial scale, such as in synaptic clefts or in the close vicinity of neuronal
 56 membranes, where ion concentrations can change dramatically within very short times [Savchenko
 57 et al., 2017; Pods, 2017]. At macroscopic tissue level, it is commonly believed that the diffusive
 58 current is much smaller than the drift current, so that even diffusive currents are typically neglected
 59 so that only the drift component (1) is considered. Then the extracellular medium is considered to
 60 be a volume conductor (VC) which greatly simplifies the calculation of extracellular potentials [Holt
 61 and Koch, 1999; Lindén et al., 2014].

62 However, if large ion-concentration gradients are present, diffusive currents could in principle
 63 affect measurable extracellular potentials [Halnes et al., 2016, 2017; Solbrå et al., 2018]. Thus in
 64 scenarios involving dramatic shifts in extracellular concentrations, such as spreading depression and
 65 related pathologies, diffusive effects are likely to be of key importance for shaping the extracellular

66 potential [Almeida et al., 2004; O'Connell and Mori, 2016]. If so, VC theory is insufficient, and
 67 computationally much more expensive electrodiffusive modeling must be used instead.

68 In this section we start with a very general assumption of how ions moving through the brain under
 69 the combined influence of electric fields and concentration gradients TVN: strange sentence? .
 70 Building on this, we then first describe several computational schemes for modelling electrodiffusive
 71 processes before we derive the fundamental equations for VC theory assuming negligible effects
 72 from diffusion.

73 2.1. Ion concentration dynamics

74 The movement of ions, that is, charged atoms or molecules, in the brain are described in terms
 75 of the flux, and there are essentially two different processes that cause ions to move in the brain,
 76 namely diffusion and electrical drift. In such electrodiffusive processes, the flux density of an ion
 77 species k is given by [Koch, 1999]:

$$\mathbf{j}_k = -D_k \nabla c_k - \frac{D_k z_k c_k}{\psi} \nabla \phi, \quad (1)$$

78 where the first term on the right is Fick's law for the diffusive flux density j_k^{diff} , and the second term
 79 is the drift flux density j_k^{drift} , which expands Fick's law in the case where the diffusing particles also
 80 move due to electrostatic forces with a mobility D_k/ψ (cf. the Einstein-relation, Mori et al. [2008]).
 81 Here D_k is the diffusion coefficient of ion species k , ϕ is the electric potential, z_k is the valency of
 82 ion species k , and $\psi = RT/F$ is defined by the gas constant (R), Faraday's constant (F) and the
 83 temperature (T). The ion concentration dynamics of a given species is then given by the Nernst-
 84 Planck continuity equation:

$$\frac{\partial c_k}{\partial t} = -\nabla \cdot \mathbf{j}_k + f_k = \nabla \cdot \left[D_k \nabla c_k + \frac{D_k z_k c_k}{\psi} \nabla \phi \right] + f_k \quad (2)$$

85 where f_k represents any source term in the system, such as e.g., an ionic transmembrane current
 86 source [Solbrå et al., 2018].

87 In order to solve a set (i.e., one for each ion species present) of equations like eq. 2, one needs
 88 an expression for the electrical potential ϕ . There are two main approaches to this. The physically
 89 most detailed approach is to use the Poisson-Nernst-Planck (PNP) formalism [Léonetti and Dubois-
 90 Violette, 1998; Léonetti et al., 2004; Lu et al., 2007; Lopreore et al., 2008; Nanninga, 2008; Pods
 91 et al., 2013; Gardner et al., 2015]. Then ϕ is determined from Poisson's equation from electrostatics,
 92

$$\nabla^2 \phi = -\rho/\epsilon, \quad (3)$$

93 where ϵ is the permittivity of the system, and ρ is the charge density associated with the ionic
 94 concentrations, as given by:

$$\rho = F \sum_k z_k c_k. \quad (4)$$

95 An alternative, more computationally efficient approach is to replace the Poisson equation with the
 96 simplifying approximation that the bulk solution is electroneutral [Mori et al., 2008; Mori, 2009; Mori
 97 and Peskin, 2009; Mori et al., 2011; Halnes et al., 2015, 2013; Pods, 2017; Niederer, 2013; O'Connell

98 and Mori, 2016; Solbrå et al., 2018; ?], which is a good approximation on spatiotemporal scales
 99 larger than micrometers and microseconds [Grodzinsky, 2011; Pods, 2017; Solbrå et al., 2018].

100 Both the PNP formalism and the electroneutral formalism allow us to compute the dynamics of
 101 ion concentrations and the electrical potential in the extracellular space of neural tissue contain-
 102 ing an arbitrary set of neuronal and glial current sources. For example, in recent work, a version
 103 of the electroneutral formalism called the Kirchhoff-Nernst-Planck (KNP) formalism was developed
 104 into a framework for computing the extracellular dynamics (of c_k and ϕ) in a 3D space surrounding
 105 morphologically complex neurons simulated with the NEURON simulation tool [Solbrå et al., 2018].
 106 However, both the PNP and electroneutral formalisms such as KNP keep track of the spatial dis-
 107 tribution of ion concentrations, and as such they require a suitable meshing of the 3D space, and
 108 numerical solutions based on finite difference- or finite element methods. In both cases, simulations
 109 can become very heavy, and for systems at a tissue level the required computational demand may
 110 be too large to be feasible. For that reason, there is much to gain from deriving a simpler frame-
 111 work where effects of ion concentration dynamics are neglected, since, for many scenarios, this may
 112 be a good approximation. Below, we will derive this simpler frameworks, i.e., the standard volume
 113 conductor (VC) theory, using the Nernst-Planck fluxes (eq. 1) as a starting point.

114 2.2. Electrodynamics

115 If we multiply eq. 1 by $F \cdot z_k$ and take the sum over all ion species, we get an expression for the
 116 net electrical current density due to all particle fluxes:

$$\mathbf{i} = - \sum_k F z_k D_k \nabla c_k - \sigma \nabla \phi \quad (5)$$

117 where the first term is the diffusive current density i^{diff} and the second term is the drift current density
 118 i^{drift} . We have here identified the conductivity σ of the medium as [Koch, 1999]:

$$\sigma = F \sum_k \frac{\tilde{D}_k z_k^2}{\psi} c_k. \quad (6)$$

119 Current conservation in the extracellular space implies that:

$$\nabla \cdot \mathbf{i} = - \sum_k F z_k D_k \nabla^2 c_k - \nabla \cdot (\sigma \nabla \phi) = -C, \quad (7)$$

120 where C denotes the current source density (CSD), reflecting e.g., local neuronal or glial transmem-
 121 brane currents. We note that this is essentially equivalent to eq. 2 at the level of single ion species,
 122 with the exception that eq. 2 contains a term $\partial c_k / \partial t$ for accumulation of ion species k , while eq. 7
 123 does *not* contain a corresponding term ($\partial \rho / \partial t$) for charge accumulation. Hence, in eq. 7 it is im-
 124 plicitly assumed that the extracellular bulk solution is electroneutral [Solbrå et al., 2018]. We note
 125 that in general, the CSD term includes both ionic transmembrane currents and transmembrane
 126 capacitive currents, and that the latter means that the local charge accumulation building up the
 127 transmembrane potential still occurs in the membrane Debye-layer.

128 Note that if we assume all concentrations to be constant in space, the diffusive term vanishes,
 129 and eq. 7 reduces to:

$$\nabla \cdot (\sigma \nabla \phi) = -C. \quad (8)$$

130 This is the standard expression used in CSD theory [Mitzdorf, 1985; Nicholson and Freeman, 1975;
 131 Pettersen et al., 2006], where spatially distributed recordings of ϕ are used to make theoretical pre-
 132 dictions of underlying current sources. When using eq. 8, it is implicitly assumed that the Laplacian
 133 of ϕ exclusively reflects transmembrane current sources, and that it is not contributed to by diffusive
 134 processes.

135 We note there are two conventions for defining the variables in eqns. 1-8, both of which are
 136 in use. The variables can be defined either relative to a tissue reference volume or relative to an
 137 extracellular reference volume. The former convention is the common convention used in volume
 138 conductor theory. Then concentrations denote the number of extracellular ions per unit tissue vol-
 139 ume, sources denote the number of ions/the net charge per unit tissue volume per second, and
 140 flux/current densities are defined per unit tissue cross-section area. Then, σ interprets as the con-
 141 ductivity experienced by the current density per tissue cross section area.

142 As eq. 7 indicates, also diffusive processes can in principle contribute to the Laplacian of ϕ , and
 143 if present, they could give rise to a non-zero Laplacian of ϕ even in the absence of neuronal sources
 144 ($C = 0$). Previous computational studies have predicted that effects of diffusion on extracellular po-
 145 tentials are not necessarily small, but tend to be very slow, meaning that they will only affect the very
 146 low-frequency components of ϕ [Halnes et al., 2016, 2017]. This is due to the diffusive current being
 147 a direct function of ion concentrations c_k , which on a large spatial scale typically vary on a much
 148 slower time scale (seconds-minutes) than the fluctuations in ϕ that we commonly are interested
 149 in (milliseconds-seconds). Furthermore, electrodes used to record ϕ typically have a lower cutoff
 150 frequency of 0.1-1 Hz [Einevoll et al., 2013a], which means that most of the tentative diffusive con-
 151 tribution will be filtered out from experimental recordings. It may therefore be a good approximation
 152 to neglect the diffusive term, except in the case of pathologically dramatic concentration variations.
 153 For the rest of this chapter, we shall do so, and assume that electrodynamics in neural tissue can be
 154 determined by eq. 8.

155 2.3. Volume conductor theory

156 In simulations of morphologically complex neurons, we typically compute a set of transmem-
 157 brane current sources for each neuronal segment [Koch, 1999]. Commonly, one assumes that the
 158 extracellular potential does not affect the neurons (i.e., no ephaptic coupling), since extracellular
 159 potentials are typically much smaller than the membrane potential of ~ 70 mV. By assuming that
 160 the tissue medium can be approximated as a volume conductor [Holt and Koch, 1999; Lindén et al.,
 161 2014], one can then use the standard CSD equation (eq. 8) to perform a forward modeling of the
 162 extracellular potential at each point in space surrounding the neuron(s).

163 If we consider the simple case of a single point-current source I_1 at the origin in an isotropic
 164 medium, the current density $\mathbf{i} = -\sigma \nabla \phi$ through a spherical shell with area $4\pi r^2$ must, due to the
 165 spherical symmetry, equal $I_1/4\pi r^2 \hat{\mathbf{r}}$. Integration with respect to r gives us:

$$\phi = \frac{I_1}{4\pi\sigma r}, \quad (9)$$

166 where r is the distance from the source.

167 If we have several point-current sources, I_1, I_2, I_3, \dots , in locations $\mathbf{r}_1, \mathbf{r}_2, \mathbf{r}_3, \dots$, their contributions

168 add up due to the linearity assumption (see sec. 2.3.2), and the potential in a point \mathbf{r} is given by:

$$\phi(\mathbf{r}) = \frac{I_1}{4\pi\sigma|\mathbf{r} - \mathbf{r}_1|} + \frac{I_2}{4\pi\sigma|\mathbf{r} - \mathbf{r}_2|} + \frac{I_3}{4\pi\sigma|\mathbf{r} - \mathbf{r}_3|} + \dots = \sum_k \frac{I_k}{4\pi\sigma|\mathbf{r} - \mathbf{r}_k|}. \quad (10)$$

169 Eq. 10 is often referred to as the point-source approximation [Holt and Koch, 1999; Lindén et al.,
170 2014], since the membrane current from a neuronal segment is assumed to enter the extracellular
171 medium in a single point. An often used further development is obtained by integrating eq. 10 along
172 the segment axis, corresponding to the transmembrane current being evenly distributed along the
173 segment axis, giving the line-source approximation [Holt and Koch, 1999; Lindén et al., 2014].

174 2.3.1. Current-dipole approximation

175 When estimating the extracellular potential far away from a volume containing a combination of
176 current sinks and sources, it can often be useful to express eq. (10) in terms of a multipole expansion.
177 That is, ϕ can be precisely described by [Nunez and Srinivasan, 2006],

$$\phi(R) = \frac{C_{\text{monopole}}}{R} + \frac{C_{\text{dipole}}}{R^2} + \frac{C_{\text{quadrupole}}}{R^3} + \frac{C_{\text{octupole}}}{R^4} + \dots, \quad (11)$$

178 when the distance R from the center of the volume to the measurement point is larger than the
179 distance from volume center to the most peripheral source [Jackson, 1998].

180 In neural tissue, there will be no current monopole contribution to the extracellular potential,
181 that is, $C_{\text{monopole}} = 0$. This follows from the requirement inherent in the cable equation that the
182 sum over all transmembrane currents, including the capacitive currents, across the neuronal surface
183 has to be zero at all points in time [Pettersen et al., 2012]. Further, the quadrupole, octupole and
184 higher-order contributions decay rapidly with distance R . Consequently, the multipole expansion
185 can be approximated by the dipole contribution for large distances, a simplification known as the
186 current-dipole approximation [Nunez and Srinivasan, 2006]:

$$\phi(\mathbf{R}) \approx \frac{C_{\text{dipole}}}{R^2} = \frac{1}{4\pi\sigma} \frac{|\mathbf{p}| \cos \theta}{R^2}. \quad (12)$$

187 Here, \mathbf{p} is the current dipole moment and θ is the angle between the current dipole moment and the
188 distance vector \mathbf{R} . The current dipole moment can be found by summing up all the position-weighted
189 transmembrane currents from a neuron [Pettersen et al., 2008, 2014; Nunez and Srinivasan, 2006]:

$$\mathbf{p} = \sum_{k=1}^N I_k \mathbf{r}_k. \quad (13)$$

191 In the case of a two-compartment neuron model (see Section 3) with a current sink $-I$ at location
192 \mathbf{r}_1 and a current source I at location \mathbf{r}_2 , the current dipole moment can be formulated as $\mathbf{p} =$
193 $-I\mathbf{r}_1 + I\mathbf{r}_2 = I(\mathbf{r}_2 - \mathbf{r}_1) = Id$, where \mathbf{d} is the distance vector between the current sink and the
194 current source, giving the dipole length d and direction of the current dipole. The current-dipole
195 approximation is applicable in the far-field limit, that is when R is much larger than the dipole length.
196 For an investigation of the applicability of this approximation for the LFP generated by a single
197 neuron, see Lindén et al. [2010].

198

199 2.3.2. Assumptions in volume conductor theory

200 The point-source approximation, eq. 10 (or the line-source version of it), and the current-dipole
201 approximation, eq. (12), represent volume conductor theory in its simplest form, and are based on a
202 set of assumptions, some of which may be relaxed for problems where it is relevant:

- 203 1. **Quasi-static approximation of Maxwell's equations:** Terms with time derivatives of the
204 electrical and magnetic fields are neglected. This approximation appears to be well-justified
205 for the relatively low frequencies relevant for brain signals, below about 10 kHz [Nunez and
206 Srinivasan, 2006].
- 207 2. **Linear extracellular medium:** Linear relationship ($\mathbf{i} = -\sigma \nabla \phi$) between the current density
208 \mathbf{i} and the electrical field, $\nabla \phi$. This is essentially Ohm's law for volume conductors, and the
209 relation is constitutive, meaning that it is observed in nature rather than derived from any
210 physical principle [Nunez and Srinivasan, 2006; Pettersen et al., 2012].
- 211 3. **Frequency-independent conductivity:** Capacitive effects in neural tissue are assumed to be
212 negligible compared to resistive effects in volume conduction. This approximation seems to be
213 justified for the relevant frequencies in extracellular recordings [Logothetis et al., 2007; Miceli
214 et al., 2017; Ranta et al., 2017], see Fig. 2. Note that it is possible to expand the formalism to
215 include a frequency-dependent conductivity [Tracey and Williams, 2011; Miceli et al., 2017].
- 216 4. **Isotropic conductivity:** The electrical conductivity, σ , is assumed to be the same in all spatial
217 directions. Cortical measurements have indeed found the conductivities to be comparable
218 across different lateral directions in cortical grey matter [Logothetis et al., 2007]. However,
219 the conductivity in the depth direction, i.e., parallel to the long apical dendrites, was found
220 to be up to 50% larger than in the lateral direction in rat barrel cortex [Goto et al., 2010].
221 Anisotropic electrical conductivities have also been found in other brain regions, for example in
222 frog cerebellum [Nicholson and Freeman, 1975] and in guinea-pig hippocampus [Holsheimer,
223 1987]. The approximation that σ is homogeneous is still often acceptable, as it normally
224 gives fairly good estimations of the extracellular potential, at least in cortical tissue [Ness
225 et al., 2015]. However, it is relatively straightforward to expand the formalism to account for
226 anisotropic conductivities [Ness et al., 2015].
- 227 5. **Homogeneous conductivity:** The extracellular medium was assumed to have the same con-
228 ductivity everywhere. Although neural tissue is highly non-homogeneous on the micrometer
229 scale [Nicholson and Syková, 1998], microscale inhomogeneities may average out on a larger
230 spatial scale, and a homogeneous conductivity seems to be a reasonable approximation within
231 cortex [Logothetis et al., 2007]. In hippocampus, however, the conductivity has been found
232 to be layer-specific [López-Aguado et al., 2001]. In situations where the assumption of a
233 homogeneous conductivity is not applicable, eq. 8 can always be solved for arbitrarily com-
234 plex geometries using numerical methods, like the Finite Element Method (FEM) [Logg et al.,
235 2012]. For some example neuroscience applications, see Moffitt and McIntyre [2005]; Frey
236 et al. [2009]; Joucla and Yvert [2012]; Haufe et al. [2015]; Ness et al. [2015]; Buccino et al.
237 [2019]; Obien et al. [2019]. For some simple non-homogeneous cases analytical solutions can
238 still be obtained, for example through the Method of Images for *in vitro* brain slices [Ness et al.,
239 2015], and the four-sphere head model for EEG signals (Sec. 5) [Næss et al., 2017].
- 240 6. **No effects from ion diffusion:** To account for diffusion of ions, one would need to compute
241 the electrodynamics of the system using one of the electrodiffusive frameworks presented in

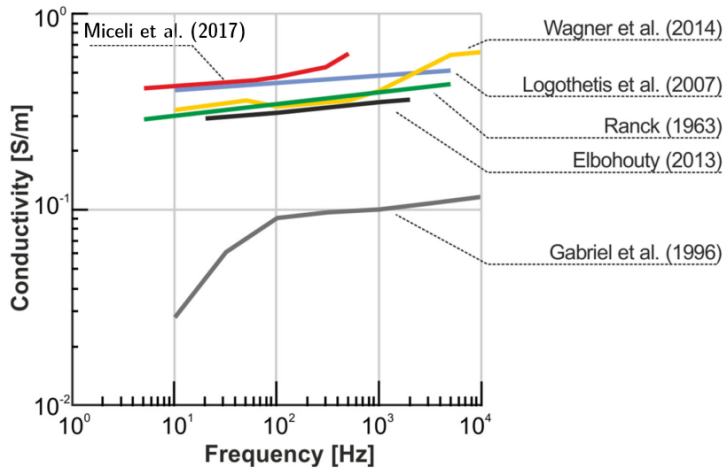


Figure 2: **Literature review of reported conductivities in various species and experimental setups.** Most studies seem to indicate a very weak frequency dependence of the extracellular conductivity, which would have a negligible effect on measured extracellular potentials [Miceli et al., 2017]. The very low and strongly frequency dependent values measured by Gabriel et al. [1996] represents an outlier, and although it has received substantial attention, it has to the best of our knowledge not been reproduced by any other study. For details about the data, see [Miceli et al., 2017], and references therein [Ranck, 1963; Gabriel et al., 1996; Logothetis et al., 2007; Elbohouty, 2013; Wagner et al., 2014].

243 Volume conductor theory is the fundament for forward modeling of extracellular potentials at
 244 different spatial scales, from extracellular spikes, LFPs and MUAs, to ECoGs and EEGs. In the
 245 following sections we shall review previous modeling works, and insights from simulating electrical
 246 potentials at these different scales. We use the software LFPy [Lindén et al., 2014; Hagen et al.,
 247 2018, 2019], which has volume conductor theory incorporated and can in principle be used to com-
 248 pute extracellular potentials on arbitrarily large spatial scales, surrounding arbitrarily large neuronal
 249 populations.

250 *2.4. Modeling electrodes*

251 The simplest and most commonly used approach when modeling extracellular recordings is to
 252 calculate the extracellular potential at single points following one of the approaches outlined above,
 253 and use this as a measure of recorded potentials. Implicitly, this assumes ideal point electrodes,
 254 that is, that the electrodes (and electrode shank) do not affect the extracellular potential and that
 255 the extracellular potential does not vary substantially over the surface of the electrodes. (This point-
 256 electrode assumption was used for all simulation examples in this chapter).

257 A numerically straightforward extension is the disc-electrode approximation where the potential
 258 is evaluated at a number of points on the electrode surface, and the average calculated [Nunez
 259 and Srinivasan, 2006; Lindén et al., 2014]. GTE: Does Nunez talk about this? TVN: Yes,
 260 eq. (5.30) in the book, however, strangely they actually use a volume integral, so maybe just re-
 261 move the reference? This approach takes into account the physical extent of the electrode, but not

any effect the electrode itself might have on the electric potential. Close to the electrode surface the electric potential will however be affected by the presence of the high-conductivity electrode contact [McIntyre and Grill, 2001; Moulin et al., 2008], and a third, and numerically much more comprehensive approach to modeling electrodes is to use the Finite Element Method (FEM) to model the electrode [Moulin et al., 2008; Ness et al., 2015], or the electrode shank [Moffitt and McIntyre, 2005; Buccino et al., 2019]. Using FEM for validation, Ness et al. [2015] found that the ideal point-electrode and disc-electrode approximations were reasonably accurate when the distance between the current sources and the recording electrode was bigger than ~ 4 times and ~ 2 times the electrode radius, respectively, indicating that the effects of the electrodes themselves are negligible in most cases [Nelson and Pouget, 2010]. The presence of large multi-contact electrode probes can, however, substantially affect the extracellular potential in its vicinity, by effectively introducing a large non-conducting volume [Mechler and Victor, 2012], and this can amplify or dampen recorded potentials from nearby cells by almost a factor of two, depending on whether the cell is in front of or behind the electrode shank [Buccino et al., 2019].

Note that for modelling current stimulation electrodes (as opposed to just recording electrodes), more complex electrode models might be needed due to electrode polarization effects [McIntyre and Grill, 2001; Martinsen and Grimnes, 2008; Joucla and Yvert, 2012].

3. Single-cell contributions to extracellular potentials

The transmembrane currents of a neuron during any neural activity can be used to calculate extracellular potentials, by applying the formalism described in Sec. 2.3, and in the simplest case eq. 10. Current conservation requires that the transmembrane currents across the entire cellular membrane at any given time sum to zero [Koch, 1999; Nunez and Srinivasan, 2006], and since an excitatory synaptic input generates a current sink (negative current), this will necessarily lead to current sources elsewhere on the cell. This implies that point neurons, that is, neurons with no spatial structure, will have no net transmembrane currents, and hence cause no extracellular potentials (Fig. 3A). The simplest neuron models that are capable of producing extracellular potentials are therefore two-compartment models, which will have two equal but opposite transmembrane currents, giving rise to perfectly symmetric extracellular potentials (Fig. 3B).

Multi-compartment neuron models mimicking the complex spatial structure of real neurons will typically give rise to complicated patterns of current sinks and sources (negative and positive currents respectively), leading to complex, but mostly dipolar-like extracellular potentials (Fig. 3C) [Einevoll et al., 2013a]. Note that this framework for calculating extracellular potentials is valid both for subthreshold and suprathreshold neural activity, that is, when a cell receives synaptic input that does not trigger, or does trigger an action potential, respectively (Fig. 3, D versus E).

4. Intra-cortical extracellular potentials from neural populations

Extracellular potentials measured within neural tissue are often split into two separate frequency domains, which reflect different aspects of the underlying neural activity. The low frequency part, that is, the local field potential (LFP), is thought to mostly reflect synaptic input to populations of pyramidal cells, while the high-frequency part, that is, the multi-unit activity (MUA), reflects the population spiking activity (Fig. 4).

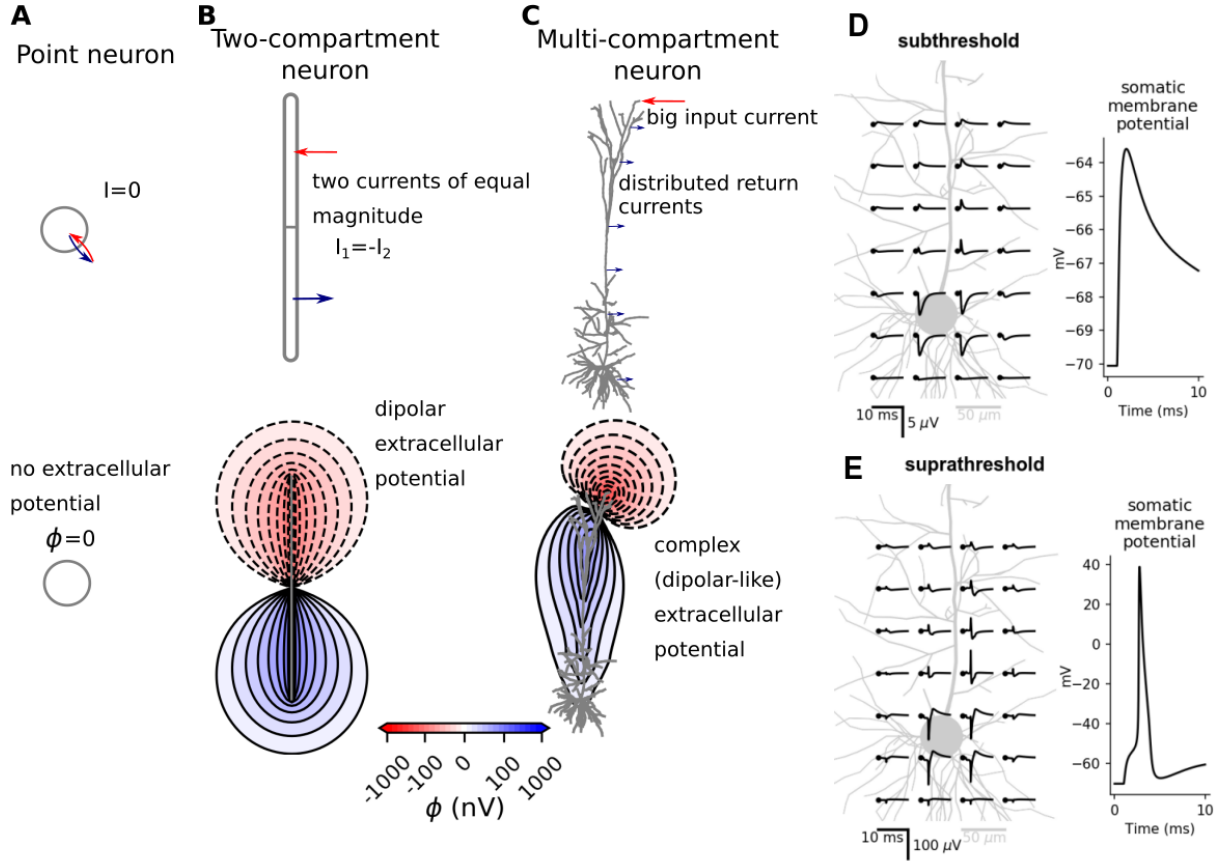


Figure 3: Single-cell contributions to the extracellular potential. **A:** Point neurons have no net currents (top), and therefore cause no extracellular potentials (bottom). **B:** Two-compartment neuron models have two opposite currents of identical magnitude (top), and cause perfectly symmetric dipolar-like extracellular potentials (bottom). **C:** Multi-compartment neuron models [Hay et al., 2011] give rise to complex source-sink patterns (top) and complex (but mostly dipolar-like) extracellular potentials (bottom). **D, E:** A single somatic synaptic input to a complex multi-compartment cell model, either subthreshold (D) or suprathreshold (E; double synaptic weight of D), illustrating that the same framework can be used to calculate both the LFP contribution from subthreshold synaptic input, and extracellular action potentials.

302 4.1. Local field potentials

303 The LFP is the low-frequency part ($\lesssim 500$ Hz) of the extracellular potentials, and it is among the
 304 oldest and most used brain signals in neuroscience [Einevoll et al., 2013a]. The LFP is expected
 305 to be dominated by synaptic inputs asymmetrically placed onto populations of geometrically aligned
 306 neurons [Nunez and Srinivasan, 2006; Lindén et al., 2011; Einevoll et al., 2013b]. In cortex and
 307 hippocampus, neurons can broadly speaking be divided into two main classes: the inhibitory in-
 308 terneurons, and the excitatory pyramidal neurons. Pyramidal neurons typically have a clear axis of
 309 orientation, that is, the apical dendrites of close-by pyramidal neurons tend to be oriented in the same
 310 direction (Fig. 4A). This geometrical alignment is important because the LFP contributions from the
 311 individual pyramidal cells also align and therefore sum constructively. For example, basal excita-
 312 tory synaptic input (Fig. 4B, time marked by red line) generates a current sink and corresponding

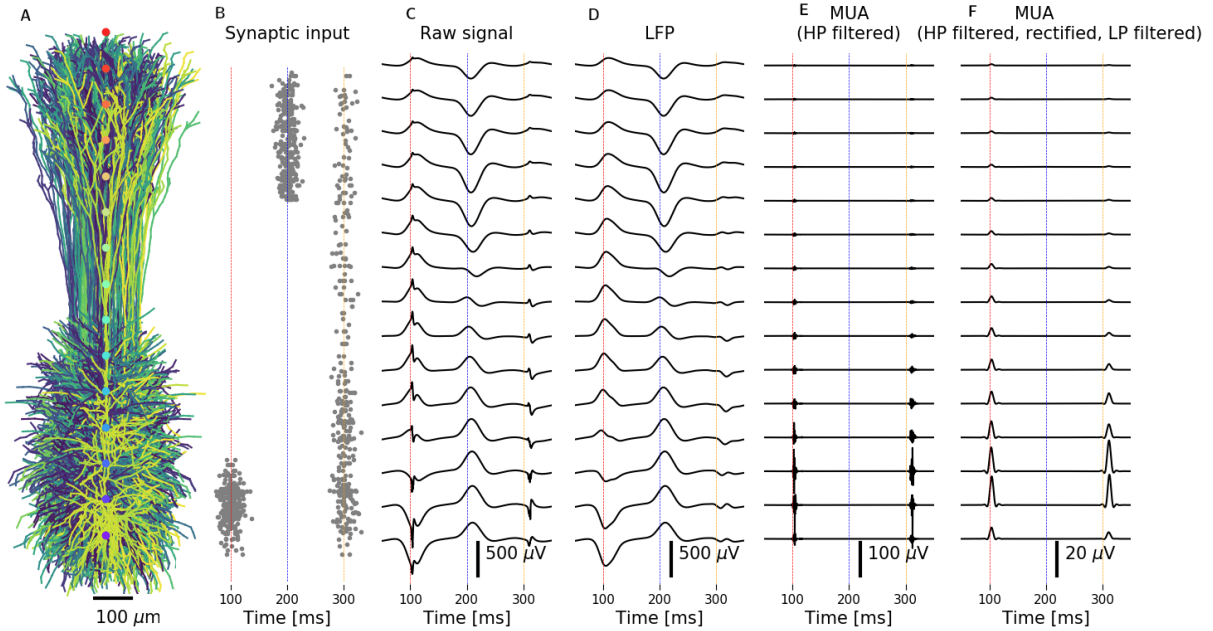


Figure 4: Extracellular potentials from different waves of synaptic input. Different brain signals from separate waves of synaptic input to 10 000 layer 5 pyramidal cells from rat [Hay et al., 2011]. **A:** A subset of 100 pyramidal cells, with the LFP electrode locations indicated in the center (colored dots). **B:** Depth-resolved synaptic inputs arrive in three waves, first targeting the basal dendrites ($t=100$ ms), then the apical dendrites ($t=200$ ms), and lastly uniformly across the entire depth ($t=300$ ms). Note that all synaptic input is pre-defined, that is, there is no network activity. **C:** The extracellular potential at different depths (corresponding to dots in panel A), including both spikes and synaptic input. **D:** The LFP, that is, a low-pass filtered version of the raw signal in C. **E:** The MUA, that is, a high-pass filtered version of the raw signal in C. **F:** Another version of the MUA which is a rectified and low-pass filtered version of the MUA signal in E. All filters were 4th order Butterworth filters in forward-backward mode [NeuroEnsemble, 2017]. For illustration purposes a relatively low cut-off frequency of 50 Hz was chosen for the LFP low-pass filter. The MUA was first high-pass filtered above 300 Hz (E and F), then rectified and low-pass filtered below 300 Hz (F).

negative LFP deflection in the basal region, and simultaneously a current source and corresponding positive LFP deflection in the apical region (Fig. 4D, time marked by red line), while apical excitatory synaptic input leads to the reversed pattern (Fig. 4B,D, time marked by blue line). Importantly, this means that excitatory input that simultaneously targets both the apical and the basal dendrite will give opposite source/sink patterns which will lead to substantial cancellation and a weak LFP contribution (Fig. 4B, D, time marked by orange line). The same arguments also apply to inhibitory synaptic inputs, with the signs of the currents and LFPs reversed.

Note that, for example, the LFP signature of apical excitatory synaptic input is inherently similar to that of basal inhibitory input, and indeed, separating between cases like this pose a real challenge in interpreting LFP signals [Lindén et al., 2010].

In contrast to pyramidal neurons, interneurons often lack any clear orientational specificity, meaning that the current dipoles from individual interneurons, which might by themselves be sizable [Lindén et al., 2010], do not align, leading to negligible net contributions to LFP signals [Mazzoni et al., 2015]. Note, however, that the interneurons may indirectly cause large LFP contributions

327 through their synaptic inputs onto pyramidal cells [Teleńczuk et al., 2017; Hagen et al., 2016].

328 It has been demonstrated that correlations among the synaptic inputs to pyramidal cells can
329 amplify the LFP signal power by orders of magnitude, with the implication that populations receiving
330 correlated synaptic input can dominate the LFP also 1-2 mm outside of the population [Lindén et al.,
331 2011; Łęski et al., 2013].

332 Somatic action potentials lasting only a few milliseconds are generally expected to contribute little
333 to cortical LFP signals [Pettersen et al., 2008; Pettersen and Einevoll, 2008; Einevoll et al., 2013a;
334 Haider et al., 2016]: Their very short duration with both positive and negative phases (Fig. 3E)
335 will typically give large signal cancellations of the contributions from individual neurons, and their
336 high frequency content is to a large degree removed from LFPs during low-pass filtering. Note,
337 however, that in the hippocampus the highly synchronized spikes found during sharp wave ripples
338 are expected to also contribute to shaping of the LFP [Schomburg et al., 2012; Luo et al., 2018].

339 Other active conductances may contribute in shaping the LFP, for example, the slower dendritic
340 calcium spikes [Suzuki and Larkum, 2017] or long-lasting after-hyperpolarization currents [Reimann
341 et al., 2013]. Further, subthreshold active conductances can also shape the LFP by molding the
342 transmembrane currents following synaptic input, and the hyperpolarization-activated cation channel
343 I_h may play a key role in this, both through asymmetrically changing the membrane conductance,
344 and by introducing apparent resonance peaks in the LFP [Ness et al., 2016, 2018].

345 4.2. MUA

346 While LFPs are thought to mainly reflect the synaptic input to large populations of pyramidal neu-
347 rons, the multi-unit activity (MUA) can be used to probe the population spiking activity [Einevoll et al.,
348 2007; Pettersen et al., 2008] (Fig. 4 E,F). In other words, the MUA holds complimentary information
349 to the LFP. In particular, this can be useful for some cell-types, like stellate cells and inhibitory
350 interneurons, which are expected to have very weak LFP contributions [Lindén et al., 2011], but might
351 still be measurable through their spiking activity. Similarly, spatially uniformly distributed synaptic
352 input to pyramidal neurons results in a negligible LFP contribution (Fig. 4C, time marked by orange
353 line), while the population might still contribute substantially to the MUA through the extracellular
354 action potentials (Fig. 4E-F, time marked by orange line).

355 5. ECoG and EEG

356 In order to measure electric potentials in the immediate vicinity of neurons, like LFP and MUA
357 signals, we need to insert sharp electrodes into the brain. This highly invasive technique is quite
358 common in animal studies, but can only be applied to humans when there is a clear medical need, for
359 example in patients with intractable epilepsy [Zangibadi et al., 2019]. However, electric potentials
360 generated by neural activity extend beyond neural tissue and can also be measured outside the
361 brain: Placing electrodes on the brain surface, as in electrocorticography (ECoG), is a technique
362 that requires some surgery. With electroencephalography (EEG), on the other hand, potentials are
363 measured non-invasively, directly on top of the scalp.

364 Since EEG electrodes are located relatively far away from the neuronal sources, the current
365 dipole approximation, eq. (12), combined with some head model, can be applied for computing EEG
366 signals [Nunez and Srinivasan, 2006; Ilmoniemi and Sarvas, 2019]. By collapsing the transmem-
367 brane currents of a neuron simulation into one single current dipole moment, see eq. (13), we can

368 calculate EEG from arbitrary neural activity (Fig. 5). The current dipole approximation is however
 369 not unproblematic to use for computing ECoG signals, as the ECoG electrodes may be located too
 370 close to the signal sources for the approximation to apply, see [Hagen et al. \[2018\]](#).

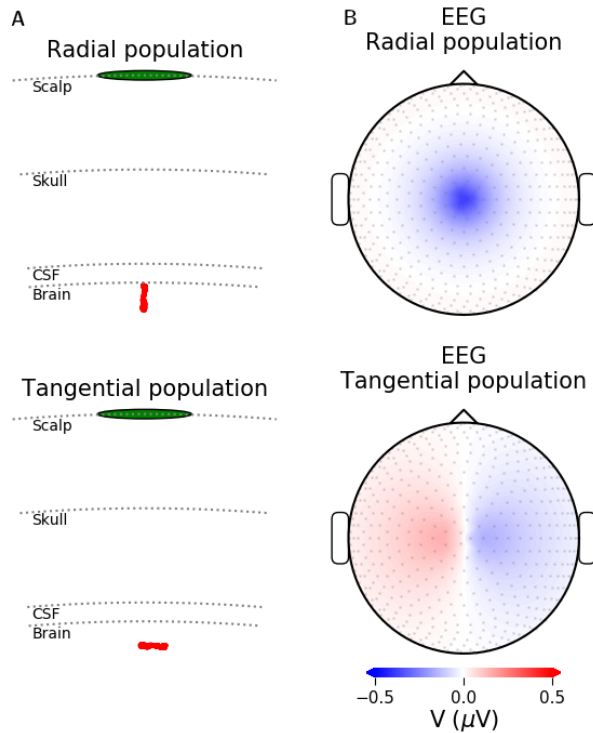


Figure 5: **EEG from apical synaptic input to population of pyramidal cells.** **A:** The four-sphere head model with two orientations of the neural population from Fig. 4, either radial, mimicking a population in a gyrus (top) or tangential, mimicking a population in a sulcus (bottom). **B:** A snapshot of the EEG signal at the head surface for apical input (time marked with blue dotted line in Fig. 4), for a radial population (top) or tangential population (bottom).

371 5.1. Head models

372 Electric potentials measured on the scalp surface will be affected by the geometries and con-
 373 ductivities of the different constituents of the head [[Nunez and Srinivasan, 2006](#)]. This can be in-
 374 corporated in EEG calculations by applying simplified or more complex head models. A well-known
 375 simplified head model is the analytical four-sphere model, consisting of four concentric shells re-
 376 presenting brain tissue, cerebrospinal fluid (CSF), skull and scalp, where the conductivity can be set
 377 individually for each shell [[Næss et al., 2017](#); [Srinivasan et al., 1998](#); [Nunez and Srinivasan, 2006](#)]
 378 (Fig. 6, Fig. 7A,B). More complex head models make use of high-resolution anatomical MRI-data
 379 to map out a geometrically detailed head volume conductor. The link between current dipoles in
 380 the brain and resulting EEG signals is determined applying numerical methods such as the finite
 381 element method [[Larson and Bengzon, 2013](#); [Logg et al., 2012](#)]. Once this link is established we
 382 can in principle insert a dipole representing arbitrary neural activity into such a model, and compute

383 the resulting EEG signals quite straightforwardly. The New York Head model is an example of one
 384 such pre-solved complex head model, see Fig. 7C,D [Huang et al., 2016].

385 The head models themselves introduce no essential frequency filtering of the EEG signal [Pfurtscheller
 386 and Cooper, 1975; Nunez and Srinivasan, 2006; Ranta et al., 2017], however, substantial spatial fil-
 387 tering will occur (Fig. 6). Additionally, the measured (or modeled) signals represent the average
 388 potential across the electrode surface, and the large electrode sizes used in ECoG/EEG recordings
 389 can have important effect on the measured signals [Nunez and Srinivasan, 2006; Hagen et al., 2018;
 390 Dubey and Ray, 2019].

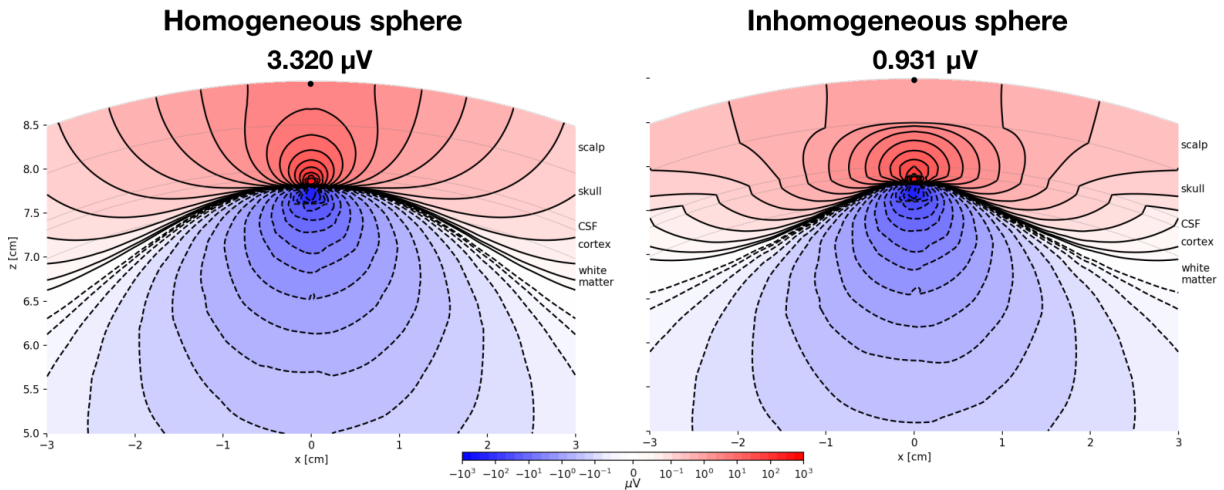


Figure 6: **Effect of head inhomogeneities.** The same current dipole will give substantially different potentials on the head surface if the different conductivities of the head is included in a FEM model [Næss et al., 2017]. Left: Homogeneous sphere, with electrical conductivity, $\sigma = 0.33 \text{ S/m}$ everywhere. Right: Standard four-sphere head model, with $\sigma_{\text{brain}} = 0.33 \text{ S/m}$, $\sigma_{\text{CSF}} = 5\sigma_{\text{brain}}$, $\sigma_{\text{skull}} = \sigma_{\text{brain}}/20$, $\sigma_{\text{scalp}} = \sigma_{\text{brain}}$.

391 6. Discussion

392 In the present chapter we have derived and applied well-established biophysical forward-modeling
 393 schemes for computing extracellular electrical potentials recorded inside and outside the brain.
 394 These electrical potentials include spikes (both single-unit and multiunit activity (MUA)), LFP, ECoG
 395 and EEG signals. The obvious application of this scheme is computation of electrical signals from
 396 neuron and network activity for comparison with experiments so that candidate models can be
 397 tested [Einevoll et al., 2019] or inferred [Goncalves et al., 2019; Skaar et al., 2020]. Another key
 398 application is the computation of benchmarking data for testing of data analysis methods such as
 399 spike sorting or CSD analysis [Denker et al., 2012].

400 Inverse modeling of recorded electrical potentials, that is, estimation of the neural sources un-
 401 derlying the signals, is inherently an ill-posed problem. This means that no unique solution for the
 402 size and position of the sources exists. However, prior knowledge about the underlying sources and
 403 how they generate the recorded signals, can be used to increase the identifiability. For example,
 404 several methods for the estimation of so-called current-source density (CSD) from LFP recordings

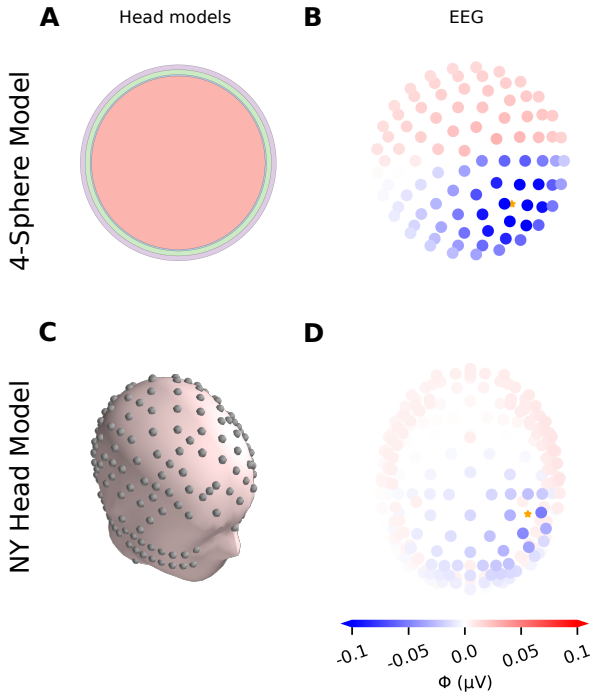


Figure 7: **The four-sphere head model and the NY Head model.** EEG signals from population dipole resulting from waves of synaptic input to 10 000 layer 5 pyramidal cells from rat [Hay et al., 2011]. **A:** The four-sphere model consisting of four concentrical shells: brain, CSF, skull and scalp. **B:** Maximum EEG signals (ϕ) on scalp surface electrodes resulting from population dipole placed at location marked by orange star, computed with the four-sphere model. **C:** Illustration of the New York Head model. **D:** EEG signals computed with the New York Head model, equivalent to panel **B**.

have been developed by building the present forward model into the CSD estimator [Pettersen et al., 2006; Potworowski et al., 2012; Cserpán et al., 2017].

The present chapter has focused on the modeling of measurements of extracellular electrical signals. Another important and related brain signal is the magnetic fields recorded outside the head in magnetoencephalography (MEG). These magnetic signals also stem from the transmembrane currents of neurons and, similar to EEG, the signal can be computed based on the current dipoles of the underlying neurons in cortex [Hämäläinen et al., 1993; Ilmoniemi and Sarvas, 2019]. The new version of our tool LFPy, which was used in generating the examples in the present chapter, thus also includes the ability to compute MEG signals [Hagen et al., 2018].

There are also other measurement modalities where detailed modeling could be pursued to allow for a more quantitative analysis of recorded data. Voltage-sensitive dye imaging (VSDI) reflects

416 area-weighted neuronal membrane potentials [Chemla and Chavane, 2012], while two-photon cal-
417 cium imaging measures the intracellular calcium dynamics [Helmchen, 2012]. Both are accessible
418 through neuronal simulations of the type used to compute electrical and magnetic signals. Func-
419 tional magnetic resonance imaging (fMRI) instead reflect blood dynamics [Bartels et al., 2012], which
420 typically are not explicitly included in neural network models.

421 **Acknowledgements**

422 This research has received funding from the European Union Horizon 2020 Framework Pro-
423 gramme for Research and Innovation under Specific Grant Agreement No. 785907 (Human Brain
424 Project SGA2), and the Research Council of Norway (Notur, nn4661k; DigiBrain, no. 248828; INCF
425 National Node, no. 269774).

426 Almeida, A. C. G., Texeira, H. Z., Duarte, M. A., Infantosi, A. F. C., March 2004. Modeling extra-
427 cellular space electrodiffusion during lea/spl tilde/o's spreading depression. IEEE Transactions on
428 Biomedical Engineering 51 (3), 450–458.

429 Bartels, A., Goense, J., Logothetis, N., Sep. 2012. Functional magnetic resonance imaging. In:
430 Brette, R., Destexhe, A. (Eds.), Handbook of Neural Activity Measurement. Cambridge University
431 Press, pp. 92–135.

432 Billeh, Y. N., Cai, B., Gratiy, S. L., Dai, K., Iyer, R., Gouwens, N. W., Abbasi-Asl, R., Jia, X., Siegle,
433 J. H., Olsen, S. R., Koch, C., Mihalas, S., Arkhipov, A., 2020. Systematic integration of structural
434 and functional data into multi-scale models of mouse primary visual cortex. Neuron.
435 URL <https://www.biorxiv.org/content/early/2019/06/06/662189>

436 Buccino, A. P., Einevoll, G. T., 2019. Mearec: a fast and customizable testbench simulator for ground-
437 truth extracellular spiking activity. bioRxiv.
438 URL <https://www.biorxiv.org/content/early/2019/07/03/691642>

439 Buccino, A. P., Kordovan, M., Ness, T. V., Merkt, B., Häfliger, P. D., Fyhn, M., Cauwenberghs, G., Rot-
440 ter, S., Einevoll, G. T., 2018. Combining biophysical modeling and deep learning for multi-electrode
441 array neuron localization and classification. Journal of Neurophysiology 120, 1212–1232.
442 URL <http://www.ncbi.nlm.nih.gov/pubmed/29847231><https://www.physiology.org/doi/10.1152/jn.00210.2018>

444 Buccino, A. P., Kuchta, M., Jæger, K. H., Ness, T. V., Berthet, P., Mardal, K.-A., Cauwenberghs, G.,
445 Tveito, A., 2019. How does the presence of neural probes affect extracellular potentials? Journal
446 of Neural Engineering 16 (2).

447 Buzsáki, G., Anastassiou, C. a., Koch, C., Jun. 2012. The origin of extracellular fields and currents—
448 EEG, ECoG, LFP and spikes. Nature reviews. Neuroscience 13 (6), 407–20.
449 URL <http://www.ncbi.nlm.nih.gov/pubmed/22595786>

450 Chemla, S., Chavane, F., Sep. 2012. Voltage-sensitive dye imaging. In: Brette, R., Destexhe, A.
451 (Eds.), Handbook of Neural Activity Measurement. Cambridge University Press, pp. 92–135.

- 452 Cserpán, D., Meszéna, D., Wittner, L., Tóth, K., Ulbert, I., Somogyvári, Z., Wójcik, D. K., Nov. 2017.
453 Revealing the distribution of transmembrane currents along the dendritic tree of a neuron from
454 extracellular recordings. *eLife* 6.
- 455 Delgado Ruz, I., Schultz, S. R., 2014. Localising and classifying neurons from high density MEA
456 recordings. *Journal of Neuroscience Methods* 233, 115–128.
457 URL <http://dx.doi.org/10.1016/j.jneumeth.2014.05.037>
- 458 Denker, M., Einevoll, G., Franke, F., Grün, S., Hagen, E., Kerr, J., Nawrot, M., Ness, T. B., Wójcik,
459 T. W. D., 2012. Report from 1st incf workshop on validation of analysis methods. Tech. rep.,
460 International Neuroinformatics Coordinating Facility (INCF).
- 461 Dubey, A., Ray, S., 2019. Cortical electrocorticogram (ecog) is a local signal. *Journal of Neuro-
462 science* 39 (22), 4299–4311.
- 463 Einevoll, G., Kayser, C., Logothetis, N., Panzeri, S., 2013a. Modelling and analysis of local field
464 potentials for studying the function of cortical circuits. *Nature Reviews Neuroscience* 14, 770–
465 785.
- 466 Einevoll, G. T., Destexhe, A., Diesmann, M., Grün, S., Jirsa, V., de Kamps, M., Migliore, M., Ness,
467 T. V., Plesser, H. E., Schürmann, F., 2019. The Scientific Case for Brain Simulations. *Neuron*
468 102 (4), 735–744.
- 469 Einevoll, G. T., Lindén, H., Tetzlaff, T., Łęski, S., Pettersen, K. H., 2013b. Local Field Potentials
470 - Biophysical Origin and Analysis. In: Quiroga, R. Q., Panzeri, S. (Eds.), *Principles of Neural
471 Coding*. CRC Press, Boca Raton, FL, Ch. 3, pp. 37–60.
- 472 Einevoll, G. T., Pettersen, K. H., Devor, A., Ulbert, I., Halgren, E., Dale, A. M., Mar. 2007. Lami-
473 nar population analysis: estimating firing rates and evoked synaptic activity from multielectrode
474 recordings in rat barrel cortex. *Journal of neurophysiology* 97 (3), 2174–90.
475 URL <http://www.ncbi.nlm.nih.gov/pubmed/17182911>
- 476 Elbohouty, M., 2013. Electrical Conductivity of Brain Cortex Slices in Seizing and Non-seizing States.
477 Ph.D. thesis, The University of Waikato.
- 478 Ellingsrud, A. J., Solbrå, A., Einevoll, G. T., Halnes, G., Rognes, M. E., 2020. Finite element simula-
479 tion of ionic electrodiffusion in cellular geometries. *Frontiers in Neuroinformatics* 14, 11.
480 URL <https://www.frontiersin.org/article/10.3389/fninf.2020.00011>
- 481 Frey, U., Egert, U., Heer, F., Hafizovic, S., Hierlemann, a., mar 2009. Microelectronic system for
482 high-resolution mapping of extracellular electric fields applied to brain slices. *Biosensors & bio-
483 electronics* 24 (7), 2191–8.
484 URL <http://www.ncbi.nlm.nih.gov/pubmed/19157842>
- 485 Gabriel, S., Lau, R. W., Gabriel, C., nov 1996. The dielectric properties of biological tissues: II.
486 Measurements in the frequency range 10 Hz to 20 GHz. *Physics in medicine and biology* 41 (11),
487 2251–69.
488 URL <http://www.ncbi.nlm.nih.gov/pubmed/8938025>

- 489 Gardner, C. L., Jones, J. R., Baer, S. M., Crook, S. M., Feb. 2015. Drift-diffusion simulation of the
490 ephaptic effect in the triad synapse of the retina. *Journal of computational neuroscience* 38 (1),
491 129–42.
492 URL <http://www.ncbi.nlm.nih.gov/pubmed/25260382>
- 493 Gold, C., Henze, D. A., Koch, C., Aug 2007. Using extracellular action potential recordings to con-
494 strain compartmental models. *J. Comput. Neurosci.* 23 (1), 39–58.
495 URL <http://dx.doi.org/10.1007/s10827-006-0018-2>
- 496 Goncalves, P. J., Lueckmann, J.-M., Deistler, M., Nonnenmacher, M., Öcal, K., Bassetto, G., Chin-
497 taluri, C., Podlaski, W. F., Haddad, S. A., Vogels, T. P., Greenberg, D. S., Macke, J. H., 2019. Train-
498 ing deep neural density estimators to identify mechanistic models of neural dynamics. *bioRxiv*.
- 499 Goto, T., Hatanaka, R., Ogawa, T., Sumiyoshi, A., Riera, J., Kawashima, R., 2010. An evaluation of
500 the conductivity profile in the somatosensory barrel cortex of wistar rats. *Journal of neurophysiology* 104 (6), 3388–3412.
- 501
- 502 Gratiy, S. L., Halnes, G., Denman, D., Hawrylycz, M. J., Koch, C., Einevoll, G. T., Anastassiou,
503 C. A., 2017. From Maxwell's equations to the theory of current-source density analysis. *European*
504 *Journal of Neuroscience* 45 (8), 1013–1023.
- 505 Grodzinsky, F., 2011. *Fields, Forces, and Flows in Biological Systems*. Garland Science, Taylor &
506 Francis Group, London & New York.
- 507 Głąbska, H., Potworowski, J., Łęski, S., Wójcik, D. K., 2014. Independent components of neural
508 activity carry information on individual populations. *PLoS One* 9 (8), e105071.
509 URL <http://dx.doi.org/10.1371/journal.pone.0105071>
- 510 Głąbska, H. T., Norheim, E., Devor, A., Dale, A. M., Einevoll, G. T., Wójcik, D. K., 2016. Generalized
511 laminar population analysis (glpa) for interpretation of multielectrode data from cortex. *Frontiers*
512 in neuroinformatics 10, 1.
- 513 Hagen, E., Dahmen, D., Stavrinou, M. L., Lindén, H., Tetzlaff, T., Van Albada, S. J., Grün, S.,
514 Diesmann, M., Einevoll, G. T., 2016. Hybrid scheme for modeling local field potentials from point-
515 neuron networks. *Cerebral Cortex* 26 (12), 4461–4496.
- 516 Hagen, E., Næss, S., Ness, T. V., Einevoll, G. T., 2018. Multimodal modeling of neural network
517 activity: computing LFP, ECoG, EEG and MEG signals with LFPy 2.0. *Front Neuroinform* 12 (92).
- 518 Hagen, E., Næss, S., Ness, T. V., Einevoll, G. T., 2019. LFPy – multimodal modeling of extracellular
519 neuronal recordings in Python. In: *Encyclopedia of Computational Neuroscience*. Springer, New
520 York, NY, p. 620286.
521 URL <http://biorxiv.org/content/early/2019/05/03/620286.abstract>
- 522 Haider, B., Schulz, D. P. A., Häusser, M., Carandini, M., 2016. Millisecond Coupling of Local Field
523 Potentials to Synaptic Currents in the Awake Visual Cortex. *Neuron* 90, 35–42.

- 524 Halnes, G., Mäki-Marttunen, T., Keller, D., Pettersen, K. H., Andreassen, O. A., Einevoll, G. T., 2016.
525 Effect of ionic diffusion on extracellular potentials in neural tissue. PLoS computational biology
526 12 (11), e1005193.
- 527 Halnes, G., Mäki-Marttunen, T., Pettersen, K. H., Andreassen, O. A., Einevoll, G. T., 2017. Ion diffu-
528 sion may introduce spurious current sources in current-source density (CSD) analysis. Journal of
529 Neurophysiology 118 (1), 114–120.
530 URL <http://jn.physiology.org/lookup/doi/10.1152/jn.00976.2016>
- 531 Halnes, G., Østby, I., Pettersen, K. H., Omholt, S. W., Einevoll, G. T., 2015. An Electrodiffusive For-
532 malism for Ion Concentration Dynamics in Excitable Cells and the Extracellular Space Surrounding
533 Them. In: Advances in cognitive neurodynamics (IV). Springer Netherlands, pp. 353–360.
534 URL http://link.springer.com/chapter/10.1007/978-94-017-9548-7_50
- 535 Halnes, G., Østby, I., Pettersen, K. H., Omholt, S. W., Einevoll, G. T., 2013. Electrodiffusive model
536 for astrocytic and neuronal ion concentration dynamics. PLoS computational biology 9 (12),
537 e1003386.
- 538 Hämäläinen, M., Hari, R., Ilmoniemi, R. J., Knuutila, J., Lounasmaa, O. V., 1993. Magnetoen-
539 cephalography?theory, instrumentation, and applications to noninvasive studies of the working
540 human brain. Reviews of modern Physics 65 (2), 413.
- 541 Haufe, S., Huang, Y., Parra, L. C., 2015. A highly detailed FEM volume conductor model based on
542 the ICBM152 average head template for EEG source imaging and TCS targeting. Conference pro-
543 ceedings : ... Annual International Conference of the IEEE Engineering in Medicine and Biology
544 Society. IEEE Engineering in Medicine and Biology Society. Annual Conference 2015, 5744–5747.
- 545 Hay, E., Hill, S., Schürmann, F., Markram, H., Segev, I., jul 2011. Models of neocortical layer 5b
546 pyramidal cells capturing a wide range of dendritic and perisomatic active properties. PLoS
547 Computational Biology 7 (7), 1–18.
548 URL <http://www.ncbi.nlm.nih.gov/pmc/articles/PMC3145650/>{&}tool=pmcentrez{&}rendertype=abstract
- 550 Helmchen, F., Sep. 2012. Calcium imaging. In: Brette, R., Destexhe, A. (Eds.), Handbook of Neural
551 Activity Measurement. Cambridge University Press, pp. 92–135.
- 552 Holsheimer, J., 1987. Electrical conductivity of the hippocampal ca1 layers and application to current-
553 source-density analysis. Experimental brain research 67 (2), 402–410.
- 554 Holt, G., Koch, C., 1999. Electrical interactions via the extracellular potential near cell bodies. Journal
555 of computational neuroscience 6, 169–184.
556 URL <http://link.springer.com/article/10.1023/A:1008832702585>
- 557 Huang, Y., Parra, L. C., Haufe, S., 2016. The New York Head—A precise standardized volume
558 conductor model for EEG source localization and tES targeting. NeuroImage 140, 150–162.
559 URL <http://dx.doi.org/10.1016/j.neuroimage.2015.12.019>

- 560 Ilmoniemi, R. J., Sarvas, J., 2019. Brain Signals - Physics and Mathematics of MEG and EEG. MIT
561 Press, Cambridge, Massachusetts; London, England.
- 562 Jackson, J. D., 1998. Classical electrodynamics, 3rd Edition. Wiley.
- 563 Joucla, S., Yvert, B., 2012. Modeling extracellular electrical neural stimulation: from basic under-
564 standing to MEA-based applications. *Journal of physiology, Paris* 106 (3-4), 146–58.
565 URL <http://www.ncbi.nlm.nih.gov/pubmed/22036892>
- 566 Koch, C., 1999. Biophysics of computation: information processing in single neurons., 1st Edition.
567 Oxford University Press: New York.
- 568 Larson, M. G., Bengzon, F., 2013. The finite element method: theory, implementation, and applica-
569 tions. Vol. 10. Springer Science & Business Media.
- 570 Łęski, S., Pettersen, K. H., Tunstall, B., Einevoll, G. T., Gigg, J., Wójcik, D. K., Dec. 2011. Inverse
571 current source density method in two dimensions: inferring neural activation from multielectrode
572 recordings. *Neuroinformatics* 9 (4), 401–25.
573 URL <http://www.ncbi.nlm.nih.gov/article/fcgi?artid=3214268&tool=pmcentrez&rendertype=abstract>
- 575 Léonetti, M., Dubois-Violette, E., Aug. 1998. Theory of Electrodynamic Instabilities in Biological
576 Cells. *Physical Review Letters* 81 (9), 1977–1980.
577 URL <http://link.aps.org/doi/10.1103/PhysRevLett.81.1977>
- 578 Léonetti, M., Dubois-Violette, E., Homblé, F., Jul. 2004. Pattern formation of stationary transcellular
579 ionic currents in *Fucus*. *Proceedings of the National Academy of Sciences of the United States of
580 America* 101 (28), 10243–8.
581 URL <http://www.ncbi.nlm.nih.gov/article/fcgi?artid=478558&tool=pmcentrez&rendertype=abstract>
- 583 Łęski, S., Lindén, H., Tetzlaff, T., Pettersen, K. H., Einevoll, G. T., 2013. Frequency dependence of
584 signal power and spatial reach of the local field potential. *PLoS Comput Biol* 9 (7), e1003137.
- 585 Lindén, H., Hagen, E., Łęski, S., Norheim, E. S., Pettersen, K. H., Einevoll, G. T., jan 2014. LFPy:
586 a tool for biophysical simulation of extracellular potentials generated by detailed model neurons.
587 *Frontiers in Neuroinformatics* 7 (41), 1–15.
588 URL <http://journal.frontiersin.org/article/10.3389/fninf.2013.00041/abstract>
- 589 Lindén, H., Pettersen, K. H., Einevoll, G. T., dec 2010. Intrinsic dendritic filtering gives low-pass
590 power spectra of local field potentials. *Journal of computational neuroscience* 29 (3), 423–44.
591 URL <http://www.ncbi.nlm.nih.gov/pubmed/20502952>
- 592 Lindén, H., Tetzlaff, T., Potjans, T. C., Pettersen, K. H., Grün, S., Diesmann, M., Einevoll, G. T., Dec.
593 2011. Modeling the spatial reach of the LFP. *Neuron* 72 (5), 859–72.
594 URL <http://www.ncbi.nlm.nih.gov/pubmed/22153380>

- 595 Logg, A., Mardal, K.-A., Wells, G., 2012. Automated solution of differential equations by the finite
596 element method: The FEniCS book. Vol. 84. Springer Science & Business Media, Berlin, Heidelberg.
597
- 598 Logothetis, N. K., Kayser, C., Oeltermann, A., sep 2007. In vivo measurement of cortical impedance
599 spectrum in monkeys: implications for signal propagation. *Neuron* 55 (5), 809–23.
600 URL <http://www.ncbi.nlm.nih.gov/pubmed/17785187>
- 601 López-Aguado, L., Ibarz, J., Herreras, O., 2001. Activity-dependent changes of tissue resistivity in
602 the ca1 region in vivo are layer-specific: modulation of evoked potentials. *Neuroscience* 108 (2),
603 249–262.
- 604 Lopreore, C. L., Bartol, T. M., Coggan, J. S., Keller, D. X., Sosinsky, G. E., Ellisman, M. H.,
605 Sejnowski, T. J., Sep. 2008. Computational modeling of three-dimensional electrodiffusion in
606 biological systems: application to the node of Ranvier. *Biophysical journal* 95 (6), 2624–35.
607 URL <http://www.ncbi.nlm.nih.gov/entrez/query.fcgi?artid=2527256&tool=pmcentrez&rendertype=abstract>
608
- 609 Lu, B., Zhou, Y. C., Huber, G. a., Bond, S. D., Holst, M. J., McCammon, J. A., Oct. 2007. Electrod-
610 iffusion: a continuum modeling framework for biomolecular systems with realistic spatiotemporal
611 resolution. *The Journal of chemical physics* 127 (13), 135102.
612 URL <http://www.ncbi.nlm.nih.gov/pubmed/17919055>
- 613 Luo, J., Macias, S., Ness, T. V., Einevoll, G. T., Zhang, K., Moss, C. F., 2018. Neural timing of stimulus
614 events with microsecond precision. *PLoS biology* 16 (10), 1–22.
- 615 Markram, H., Muller, E., Ramaswamy, S., Reimann, M. W., Abdellah, M., Sanchez, C. A., Ailamaki,
616 A., Alonso-Nanclares, L., Antille, N., Arsever, S., et al., 2015. Reconstruction and simulation of
617 neocortical microcircuitry. *Cell* 163 (2), 456–492.
- 618 Martinsen, Ø. G., Grimnes, S., 2008. Bioimpedance and Bioelectricity Basics. Academic Press; 2
619 edition.
620 URL <http://www.amazon.com/Bioimpedance-Bioelectricity-Basics-Second-Edition/dp/0123740045>
- 622 Mazzoni, A., Lindén, H., Cuntz, H., Lansner, A., Panzeri, S., Einevoll, G. T., 2015. Computing
623 the local field potential (lfp) from integrate-and-fire network models. *PLoS Comput Biol* 11 (12),
624 e1004584.
- 625 McIntyre, C. C., Grill, W. M., Mar. 2001. Finite Element Analysis of the Current-Density and Electric
626 Field Generated by Metal Microelectrodes. *Annals of Biomedical Engineering* 29 (3), 227–235.
627 URL <http://www.springerlink.com/openurl.asp?id=doi:10.1114/1.1352640>
- 628 Mechler, F., Victor, J. D., Jun. 2012. Dipole characterization of single neurons from their extracellular
629 action potentials. *Journal of computational neuroscience* 32(1), 73–100.
630 URL <http://www.ncbi.nlm.nih.gov/pubmed/21667156>

- 631 Miceli, S., Ness, T. V., Einevoll, G. T., Schubert, D., 2017. Impedance spectrum in cortical tissue:
632 Implications for propagation of lfp signals on the microscopic level. *eNeuro* 4 (1).
633 URL <https://www.eneuro.org/content/4/1/ENEURO.0291-16.2016>
- 634 Mitzdorf, U., 1985. Current source-density method and application in cat cerebral cortex: investiga-
635 tion of evoked potentials and eeg phenomena. *Physiological reviews* 65 (1), 37–100.
- 636 Moffitt, M. a., McIntyre, C. C., sep 2005. Model-based analysis of cortical recording with silicon
637 microelectrodes. *Clinical neurophysiology* 116 (9), 2240–50.
638 URL <http://www.ncbi.nlm.nih.gov/pubmed/16055377>
- 639 Mori, Y., 2009. From three-dimensional electrophysiology to the cable model: an asymptotic study.
640 arXiv preprint arXiv:0901.3914, 1–39.
641 URL <http://arxiv.org/abs/0901.3914>
- 642 Mori, Y., Fishman, G. I., Peskin, C. S., Apr. 2008. Ephaptic conduction in a cardiac strand model
643 with 3D electrodiffusion. *Proceedings of the National Academy of Sciences of the United States
644 of America* 105 (17), 6463–8.
645 URL <http://www.ncbi.nlm.nih.gov/pmc/articles/PMC2359793/>&tool=pmcentrez&rendertype=abstract
- 647 Mori, Y., Liu, C., Eisenberg, R. S., 2011. A Model of Electrodiffusion and Osmotic Water Flow and
648 its Energetic Structure. arXiv preprint arXiv:1101.5193.
- 649 Mori, Y., Peskin, C., 2009. A numerical method for cellular electrophysiology based on the electrod-
650 iffusion equations with internal boundary conditions at membranes. *Communications in Applied
651 Mathematics and Computational Science* 4.1, 85–134.
652 URL <http://msp.org/camcos/2009/4-1/p04.xhtml>
- 653 Moulin, C., Glière, A., Barbier, D., Joucla, S., Yvert, B., Mailley, P., Guillemaud, R., Feb. 2008. A new
654 3-D finite-element model based on thin-film approximation for microelectrode array recording of
655 extracellular action potential. *IEEE transactions on bio-medical engineering* 55 (2 Pt 1), 683–92.
656 URL <http://www.ncbi.nlm.nih.gov/pubmed/18270005>
- 657 Næss, S., Chintaluri, C., Ness, T. V., Dale, A. M., Einevoll, G. T., Wójcik, D. K., 2017. Corrected
658 Four-Sphere Head Model for EEG Signals. *Frontiers in Human Neuroscience* 11 (October), 1–7.
659 URL <http://journal.frontiersin.org/article/10.3389/fnhum.2017.00490/full>
- 660 Nanninga, P., 2008. A computational neuron model based on Poisson-Nernst-Planck theory.
661 ANZIAM Journal 50, 46–59.
662 URL <http://journal.austms.org.au/ojs/index.php/anziamj/article/view/1390>
- 663 Nelson, M. J., Pouget, P., may 2010. Do electrode properties create a problem in interpreting local
664 field potential recordings? *Journal of neurophysiology* 103 (5), 2315–7.
665 URL <http://www.ncbi.nlm.nih.gov/pubmed/20220081>
- 666 Ness, T. V., Chintaluri, C., Potworowski, J., Łęski, S., Głabska, H., Wójcik, D. K., Einevoll, G. T.,
667 2015. Modelling and Analysis of Electrical Potentials Recorded in Microelectrode Arrays (MEAs).

- 668 Neuroinformatics 13 (4), 403–426.
669 URL <http://link.springer.com/10.1007/s12021-015-9265-6>
- 670 Ness, T. V., Remme, M. W. H., Einevoll, G. T., 2016. Active subthreshold dendritic conductances
671 shape the local field potential. Journal of Physiology 594 (13), 3809–3825.
- 672 Ness, T. V., Remme, M. W. H., Einevoll, G. T., 2018. h-Type Membrane Current Shapes the Local
673 Field Potential from Populations of Pyramidal Neurons. Journal of Neuroscience 38 (26), 6011–
674 6024.
675 URL <http://www.jneurosci.org/lookup/doi/10.1523/JNEUROSCI.3278-17.2018>
- 676 NeuroEnsamble, 2017. Elephant - electrophysiology analysis toolkit.
677 URL <https://github.com/NeuralEnsemble/elephant>
- 678 Nicholson, C., Freeman, J. A., 1975. Theory of current source-density analysis and determination of
679 conductivity tensor for anuran cerebellum. Journal of Neurophysiology 38 (2), 356–368.
- 680 Nicholson, C., Syková, E., may 1998. Extracellular space structure revealed by diffusion analysis.
681 Trends in neurosciences 21 (5), 207–15.
682 URL <http://www.ncbi.nlm.nih.gov/pubmed/9610885>
- 683 Niederer, S., jan 2013. Regulation of ion gradients across myocardial ischemic border zones: a
684 biophysical modelling analysis. PloS one 8 (4), e60323.
685 URL <http://www.ncbi.nlm.nih.gov/pmc/articles/PMC3618345/>{&}tool=pmcentrez{&}rendertype=abstract
- 687 Nunez, P. L., Srinivasan, R., 2006. Electric Fields of the Brain. Oxford University Press, New York.
- 688 Obien, M. E. J., Hierlemann, A., Frey, U., 2019. Accurate signal-source localization in brain slices by
689 means of high-density microelectrode arrays. Scientific Reports 9 (1), 1–19.
- 690 O'Connell, R., Mori, Y., Oct 2016. Effects of glia in a triphasic continuum model of cortical spreading
691 depression. Bulletin of Mathematical Biology 78 (10), 1943–1967.
692 URL <https://doi.org/10.1007/s11538-016-0206-9>
- 693 Pettersen, K. H., Devor, A., Ulbert, I., Dale, A. M., Einevoll, G. T., Jun. 2006. Current-source density
694 estimation based on inversion of electrostatic forward solution: effects of finite extent of neuronal
695 activity and conductivity discontinuities. Journal of neuroscience methods 154 (1-2), 116–33.
696 URL <http://www.ncbi.nlm.nih.gov/pubmed/16436298>
- 697 Pettersen, K. H., Einevoll, G. T., Feb. 2008. Amplitude variability and extracellular low-pass filtering
698 of neuronal spikes. Biophysical journal 94 (3), 784–802.
699 URL <http://www.ncbi.nlm.nih.gov/pmc/articles/PMC2186261/>{&}tool=pmcentrez{&}rendertype=abstract
- 701 Pettersen, K. H., Hagen, E., Einevoll, G. T., Jun. 2008. Estimation of population firing rates and cur-
702 rent source densities from laminar electrode recordings. Journal of computational neuroscience
703 24 (3), 291–313.
704 URL <http://www.ncbi.nlm.nih.gov/pubmed/17926125>

- 705 Pettersen, K. H., Lindén, H., Dale, A. M., Einevoll, G. T., 2012. Extracellular spikes and csd. In: 706 Brette, R., Destexhe, A. (Eds.), *Handbook of Neural Activity Measurement*. Cambridge University 707 Press, pp. 92–135.
- 708 Pettersen, K. H., Lindén, H., Tetzlaff, T., Einevoll, G. T., Nov. 2014. Power laws from linear neuronal 709 cable theory: power spectral densities of the soma potential, soma membrane current and 710 single-neuron contribution to the EEG. *PLoS computational biology* 10 (11), e1003928.
711 URL <http://www.ncbi.nlm.nih.gov/pmc/articles/PMC4230751/>&tool=pmcentrez&rendertype=abstract
- 713 Pfurtscheller, G., Cooper, R., 1975. Frequency dependence of the transmission of the EEG from 714 cortex to scalp. *Electroencephalography and Clinical Neurophysiology* 38 (1), 93–96.
- 715 Pods, J., 2017. A comparison of computational models for the extracellular potential of neurons. 716 *Journal of Integrative Neuroscience* 16 (1), 19–32.
- 717 Pods, J., Schönke, J., Bastian, P., Jul. 2013. Electrodiffusion models of neurons and extracellular 718 space using the Poisson-Nernst-Planck equations—numerical simulation of the intra- and extra- 719 cellular potential for an axon model. *Biophysical journal* 105 (1), 242–54.
720 URL <http://www.ncbi.nlm.nih.gov/pmc/articles/PMC3703912/>&tool=pmcentrez&rendertype=abstract
- 722 Potworowski, J., Jakuczun, W., Lęski, S., Wójcik, D., feb 2012. Kernel current source density method. 723 *Neural computation* 24 (2), 541–75.
724 URL <http://www.ncbi.nlm.nih.gov/pubmed/22091662>
- 725 Ranck, J. B., 1963. Specific impedance of rabbit cerebral cortex. *Experimental Neurology* 7 (2), 726 144–152.
727 URL <http://www.sciencedirect.com/science/article/B6WFG-4GYGC4V-5/2-fb431eaa3c8ad95684a2c909cda91241>
- 729 Ranta, R., Le Cam, S., Tyvaert, L., Louis-Dorr, V., 2017. Assessing human brain impedance using 730 simultaneous surface and intracerebral recordings. *Neuroscience* 343, 411–422.
- 731 Reimann, M. W., Anastassiou, C. A., Perin, R., Hill, S. L., Markram, H., Koch, C., jul 2013. A 732 biophysically detailed model of neocortical local field potentials predicts the critical role of active 733 membrane currents. *Neuron* 79 (2), 375–390.
734 URL <http://linkinghub.elsevier.com/retrieve/pii/S0896627313004431>
- 735 Savtchenko, L. P., Poo, M. M., Rusakov, D. A., 2017. Electrodiffusion phenomena in neuroscience: 736 A neglected companion.
737 URL <http://dx.doi.org/10.1038/nrn.2017.101>
- 738 Schomburg, E. W., Anastassiou, C. A., Buzsaki, G., Koch, C., aug 2012. The Spiking Component 739 of Oscillatory Extracellular Potentials in the Rat Hippocampus. *Journal of Neuroscience* 32 (34), 740 11798–11811.
741 URL <http://www.jneurosci.org/cgi/doi/10.1523/JNEUROSCI.0656-12.2012>

- 742 Skaar, J.-E. W., Stasik, A. J., Hagen, E., Ness, T. V., Einevoll, G. T., 2020. Estimation of neural
743 network model parameters from local field potentials (lfps). PLoS Computational Biology.
- 744 Solbrå, A., Bergersen, A. W., van den Brink, J., Malthe-Sørenssen, A., Einevoll, G. T., Halnes, G.,
745 2018. A Kirchhoff-Nernst-Planck framework for modeling large scale extracellular electrodiffusion
746 surrounding morphologically detailed neurons. PLoS Computational Biology 14 (10), 1–26.
- 747 Srinivasan, R., Nunez, P. L., Silberstein, R. B., 1998. Spatial filtering and neocortical dynamics:
748 estimates of eeg coherence. IEEE transactions on Biomedical Engineering 45 (7), 814–826.
- 749 Sterratt, D., Graham, B., Gillies, A., Willshaw, D., 2011. Principles of computational modelling in
750 neuroscience. Cambridge University Press.
- 751 Suzuki, M., Larkum, M. E., 2017. Dendritic calcium spikes are clearly detectable at the cortical
752 surface. Nature Communications 8 (276), 1–10.
753 URL <http://dx.doi.org/10.1038/s41467-017-00282-4>
- 754 Teleńczuk, B., Dehghani, N., Le Van Quyen, M., Cash, S. S., Halgren, E., Hatsopoulos, N. G.,
755 Destexhe, A., 2017. Local field potentials primarily reflect inhibitory neuron activity in human and
756 monkey cortex. Scientific reports 7, 40211.
- 757 Tracey, B., Williams, M., 2011. Computationally efficient bioelectric field modeling and effects of
758 frequency-dependent tissue capacitance. Journal of Neural Engineering 8 (3).
- 759 Wagner, T., Eden, U., Rushmore, J., Russo, C. J., Dipietro, L., Fregni, F., Simon, S., Rotman, S.,
760 Pitskel, N. B., Ramos-Estebanez, C., Pascual-Leone, A., Grodzinsky, A. J., Zahn, M., Valero-
761 Cabré, A., jan 2014. Impact of brain tissue filtering on neurostimulation fields: a modeling study.
762 NeuroImage 85 (3), 1048–57.
763 URL <http://www.ncbi.nlm.nih.gov/pubmed/23850466>
- 764 Zangiabadi, N., Ladino, L. D., Sina, F., Orozco-Hernández, J. P., Carter, A., Téllez-Zenteno, J. F.,
765 2019. Deep brain stimulation and drug-resistant epilepsy: a review of the literature. Frontiers in
766 Neurology 10.